InSb DRO Array Characteristics

W. J. Forrest, J. L. Pipher, Z. Ninkov, J. D. Garnett
Department of Physics and Astronomy
University of Rochester, Rochester, NY 14627

Abstract: We have tested 58×62 low-doped InSb diode arrays bonded to MOSFET readouts for their performance potential in a low background space environment. The arrays were constructed by SBRC under a contract from NASA. Of primary concern were the quantum efficiency, dark current and read noise. The quantum efficiency (45% at 3.3μm) and dark current ($< 2.4e^-/s$) were found to be adequate for the SIRTF experiments, while the read noise (200 e^- RMS) was found to be wanting. More subtle concerns, such as image quality, linearity/calibratibility and flat fielding were also investigated. In these respects the arrays appear to be well suited for the high sensitivity, photometric accuracy, and image clarity demanded by the SIRTF experiments.

Introduction

The Infrared Array Camera (IRAC) and Infrared Spectrometer (IRS) on NASA's Space Infrared Telescope Facility (SIRTF) experiment require high quality, large format detector arrays for the 2 to 5 μm spectral region. Under contract from NASA, the IRAC team approached Santa Barbara Research Center (SBRC) to produce the first generation arrays, optimized for space. InSb photovoltaic material was selected, being the most mature technology with the best immediate prospects for high performance. Low doping ($2\times10^{14}/\mathrm{cm}^3$, rather than the standard $1-2\times10^{15}/\mathrm{cm}^3$) was chosen in order to reduce the dark current at low temperatures and reduce the detector capacitance, leading to reduced read noise. The goals for these detectors were high quantum efficiency ($> 50\%$), low dark current ($< 2e^-/\mathrm{sec}$), low read noise ($< 100e^- RMS$), excellent imaging qualities, stable (calibratible) output, and resilience to the SIRTF radiation environment. The research team at the University of Rochester has been responsible for the test and evaluation of these arrays, described below. The 58×62 InSb detectors and CRC 228 MOSFET direct readout have been described in detail by Fowler *et al.* (1987) and Orias *et al.* (1986). A brief description of our detector test station has been given by Ninkov *et al.* (1987).

Quantum Efficiency/Detector Thickness

The first array tested, SCA 1, displayed a common fault with these detectors, loss of quantum efficiency (QE) as temperature is lowered. In fig. 1 is shown a comparison of the 3.3μm QE at 8K and 31K. In fig. 2 this data is shown as a histogram. It can be seen

that at 31K, the QE is quite respectable, about 45%, with a relatively narrow distribution about the mean. However at 8K, the average QE drops to 20%, with a severe loss of QE on the left side of the array. Since the dark current was too high, about 6 aA ($38e^-/s$) at 31K, we consider this particular array unsuitable for SIRTF.

Figure 3 compares the QE of SCA 2 to SCA 1 at low temperatures. It can be seen that SCA 2 is much superior at maintaining QE at low temperatures. From the histogram in fig. 4, the average QE is 32% using -1.5V on the detector gates (VGATE, see Fowler *et al.* (1987) and Orias *et al.* (1987) for a description) and 43% with -2.3V at 10K. Figure 5 shows the ratio of a 10K flat field to a 7K flat field at 3.3μm. It can be seen that there is some die-off of QE with lowered temperature, and it is concentrated in the lower right corner, where the QE is lowest. For this array, there is a temperature, around 10K, where the quantum efficiency is acceptably high, yet the dark current (next section) remains acceptably low.

The loss of quantum efficiency with decreased temperature is evidently due to a decrease in the mean free path of the charge carriers in the InSb. Either the mobility and/or the lifetime of the carriers is too small. We suspect low temperature traps, either crystal defects or impurities, may cause this. If the mean free path is less than the distance the carriers have to travel before collection by the pn junction, then the charge may never show up in the external circuit. Since the absorption depth for 2-5 μm photons is only 1-2 μm in InSb (Sze, 1981, p.751), the carriers have to traverse nearly the full thickness of InSb, about 10μm for these detectors, before reaching the depletion region at the pn junction (which is only about a few μm deep).

We have discovered an interesting interference phenomenon which, we believe, allows us to measure the InSb thickness directly, and test the above ideas. Figure 6 shows data on SCA 2 detector, showing interference effects. The flat field through the narrow 4.67μm filter (4% resolution) shows a subtle pattern of light and dark ridges, most noticeable at the left of the array. The 22% resolution 3.75μm flat field, on the top left, shows no such effect. (We have looked for the effect using a 3.75μm 1% filter and don't see it - so it is primarily a wavelength dependent phenomenon). Dividing the 4.67μm image by the 3.75μm image removes the large gradient and other structure in the flat field and accentuates the interference pattern. At least 8 fringes may be seen, most prominent and closer together on the left side. We interpret these fringes as interference between incident and reflected radiation at the top surface of the InSb. A maximum in intensity will be observed whenever the thickness t is an integral (m) multiple of the quantity $\lambda/2n = 0.6\mu$m, where λ is the wavelength and $n = 3.8$ is the index of refraction of InSb. $m = 1, 2, 3, \ldots$ is the order of the interference:

$$t = m\frac{\lambda}{2n} \tag{1}$$

We interpret the fringes as indicating a wedge in the InSb thickness, with each fringe indicating an increase in thickness of about $0.6\mu m$. For SCA 2, we believe the thin side is on the left, where the fringes can be seen most easily. Since the penetration depth of 4.67μm photons is only about 2μm, fringes can only be seen clearly in fairly thin material. This is also the side with the best quantum efficiency, which we expect for thinner material. By counting fringes, we conclude that this detector has at least 5μm of wedge from the

left side to the right. We draw attention to the curve of the fringes at the upper and lower left corners, indicating "turned down corners", which is what one might expect from the mechanical thinning method used by SBRC.

This interpretation is strengthened and extended by measurements made on the FPA 72 detector. Here we used our 1% resolution CVF (circular variable filter) to investigate the fringing as a function of wavelength. In fig. 7, the data at 4.5μm and 3.3μm is compared. The fringes are not as pronounced as for SCA 2, probably at least partly due to the AR coating on this array, as well as the shorter wavelength employed. However, they can still be seen in the 4.5μm/3.3μm ratio image; again we point out the curvature of the fringes in the upper and lower left corners, indicating "turned down corners". Also we interpret the left side as being thinner, since the fringes are much more visible there. By repeating this at 4.4μm (figure 8), we learn a lot. First, we note that the fringes move to the right as we increase wavelength from 4.4 to 4.5μm. This means the thickness increases toward the right, confirming the speculations made above. The amount of fringe shift for a given wavelength change compared to the fringe spacing gives the order m and hence the thickness through:

$t_1 = m\lambda_1/2n$	thickness at fringe peak of wavelength λ_1
$t_2 = m\lambda_2/2n$	thickness at fringe peak of wavelength λ_2
$t_3 = (m+1)\lambda_1/2n$	thickness at next fringe peak, wavelength λ_1

These can be combined to give:

$$m = \frac{\lambda_1}{\lambda_1 - \lambda_2} \frac{t_1 - t_2}{t_1 - t_3} \tag{2}$$

and assuming a linear wedge, the thicknesses can be replaced by the x displacement on the array:

$$m = \frac{\lambda_1}{\lambda_1 - \lambda_2} \frac{x_1 - x_2}{x_1 - x_3} \tag{3}$$

Using the following data for the first three bright fringes named a, b, and c on the left side of the array approximately half way down at row 30, where the fringes are nearly vertical):

Table. Fringes Crossing Row 30

$\lambda(\mu m)$	Fringe peak (column # = x)		
	a	b	c
4.4	8	16	25
4.5	10	17.5	28

gives an average fringe shift of $< x_1 - x_2 >$ of 2.17 pixels, for a wavelength difference $(\lambda_2 - \lambda_1)$ of $0.1\mu m$. The average fringe spacing normalized by the wavelength $< x_3 - x_1 > /\lambda$ is 1.97 pixels/μm. Inserting these values in equation (3) gives m=11.02 for the fringe crossing row 30, column 16 at 4.4μm (fringe b above). The very small deviation of the

calculated m value from an integer is taken as further support for the assumptions used here. (Our convention is rows 1 through 58 starting at the top and columns 1 through 62 starting at the left of all the images shown). From the order $m = 11$ at row 30 column 16, the thickness is determined to be 6.4μm at that position. All the other fringes can now be interpreted as iso-thickness contours, each separated by 0.6 μm, as shown in fig. 8. From this figure, it can be seen that the good side of the array (upper left corner), which maintains high QE at low temperatures, is about 5μm thick, while the poorer side (lower right corner) is about 10μm thick. Thus we conclude that even if the carrier mean free path at low temperatures can't be improved in future generations of InSb arrays, good QE performance can be achieved if the thickness is tightly controlled to $5 \pm 1\mu$m everywhere.

"Tree Rings" in Flat Fields

In all of the low and high doped InSb arrays we have tested, there is a regular pattern of bright and dark markings in the flat fields, reminding one of tree rings with the center of the tree off the array. Examples can be seen in figs. 1 and 3. We have been informed by the manufacturer of the InSb starting material that the Czochralski growth method they employ will lead to doping variations in swirling circular patterns, called by them "beach lines." It is not immediately obvious, however, how doping variations can lead to flat-field variations, since the QE should be only weakly dependent on doping (InSb is an intrinsic semiconductor). We now believe the tree rings do not represent QE variations, but rather responsivity variations caused by capacitance variations. The capacitance C of an InSb diode varies as $\sqrt{n}$, where n is the doping concentration. Since the output voltage V will be roughly given by:

$$V = Q/C \tag{4}$$

where Q is the charge collected, a variation in C will cause a variation in the output voltage, leading to tree rings. The bright rings are lower doped, lower capacitance regions and vice-versa.

For four of the more prominent tree rings on SCA 2, the peak-to-peak variation is about 25%. The total dynamic capacitance is about 0.5 pF at the 350mV of back-bias that we employed, and we estimate the fixed contribution of 0.23 pF from the detector gate and MOSFET gate. To get this much signal variation requires a detector capacitance variation from 0.21 to 0.33 pF. Taking the nominal doping level as $2 \times 10^{14}/\mathrm{cm}^3$, from the manufacturer, this implies the doping varies from 1.2 to $3.0 \times 10^{14}/\mathrm{cm}^3$, rather than the much more modest variation of $1.7 - 2.3 \times 10^{14}/\mathrm{cm}^3$ or less we had originally been told by the vendor.

Fortunately, the tree rings are very stable and hence easy to calibrate out (see fig. 5 for instance). They represent primarily a nuisance, and not a fundamental limit for SIRTF applications. We do recommend that in the future generations, the doping variations be kept to $\pm 15\%$ peak to peak rather than the present $\pm 50\%$.

Effect of VGATE on QE

The following table gives a summary of QE measurements on various low- doped arrays as a function of VGATE and temperature. We report the average QE of the working pixels, always > 90% of the total. The wavelength is 3.3μm, near the center of IRAC Band I and the short wavelength spectrometer of the IRS:

SCA 01 (non AR coated)

55% at 31K, detector gate = -0.2V
27% at 8 K, detector gate = -0.5V

SCA 02 (non AR coated)

gate:		-1.5V	-2.3V
T=	10K	32%	43%
	7K	25%	

FPA 72 (AR coated)

gate:		-2.0V	-2.3V	-2.4V	-2.5V
T=	13K		52%		
	10K				52%
	9K	36%	47%	50%	

The FPA 72 data, which were all taken on 6 July 1988, show the trend with detector gate most clearly. The data at 9 and 10K are plotted in fig. 9. The SCA 02 data for the different gate voltages were taken in Aug. 1987 (-1.5Vgate) and May 1988 (-2.3Vgate).

This is not the whole story, as we have attempted to reproduce the variation seen with FPA 72 and saw little or no variation of QE with VGATE. Re-checking the 6 July 1988 data indicates little doubt that the effect was real at that time, though a little less pronounced than shown in the figure. We conclude that the QE variation with VGATE depends also on the history of the VGATE setting, i.e. whether the gate voltages were -2.0, -2.3, -2.4, -2.5 or cycled -2.0, +2.0, -2.3, +2.0, -2.4, +2.0, -2.5. The +2.0 intermediate VGATEs are sometimes used to reset the array.

Dark Current

The extremely low backgrounds anticipated for SIRTF require correspondingly low dark currents, in order to achieve background limited performance. A key element of our development of InSb detectors was the desire to minimize the dark current. The following tables show typical backgrounds in space and backgrounds we have seen at the telescope:

TABLE 1: TYPICAL BACKGROUNDS IN SPACE (ZODIACAL LIGHT)

SIRTF Effective Area $4.9 \times 10^3 \mathrm{cm}^2$, Pixel diameter = $2.4\lambda/D$

Wavelength (μm)	$\Delta\lambda$ (μm)	Background (photons/sec)	pixel diameter (arc sec)
2.1	0.6	6.8	1.2
3.54	1.1	12.8	2.0
4.6	1.4	85.2	2.6
12.6	3.8	1.4×10^4	7.0
26.9	8.1	1.1×10^6	15

TABLE 2: BACKGROUNDS SEEN ON MAUNA KEA

(f/14, 76 μm pixels, 1 airmass)

Filter	Wavelength (μm)	$\Delta\lambda$ (μm)	Background (electrons/sec)	Primary Source
J	1.23	0.23	80-800	OH emission
H	1.65	0.32	500-5000	OH emission
K	2.23	0.41	2500-3000	telescope thermal emission
1% CVF	2.08	0.02	60	OH emission
1% CVF	2.12	0.02	100	OH emission

It can be seen that backgrounds approaching those anticipated in space are occasionally reached in the near IR at a ground based telescope, especially when observing through our 1% resolution CVF. The OH emission is highly variable on short time scales, as indicated for the J and H bands above. The actual photon background, incident on the telescope, is probably about a factor of 4-8 higher than the electrons/sec seen at the detectors.

From table 1, we conclude a dark current less than a few e^-/s is desirable. For SCA 2, the dark current is very low. In fact, we have not been able to detect it convincingly at 7K or 10K. The dark charge collected in 500 sec is given in fig. 10. The data were generated by subtracting a 500 sec integration from a 0.1 sec integration. The dark charge was actually negative, i.e. less, apparently, in the 500 sec than the 0.1 sec. This is attributed to a small offset in the whole output of the array (about -400 electrons). Taking 3 times this value as a conservative limit on the true dark charge gives a limit of $< 2.4e^-$/ s (0.4 aA) for the dark current. The spread in dark charge shown in the figure corresponds to an RMS noise of about 300 e^- for this data.

A grey scale image of dark current at 10K is shown in fig. 11. No true dark current could be detected in the central 95% of the array. Since the integration time was shorter, 167 sec., the upper limit on dark current is somewhat higher, $< 6e^-$/sec, here. There is considerable dark current in row 1 and, especially, column 62 at this temperature. Also noticeable is a glow in the lower right corner of the array, amounting to some 100's of e^- /sec. This is the region where the output amplifiers are located. We have eliminated this glow recently by reducing VGGUC and VDD.

Read Noise

A read noise of $< 100e^-$ RMS is required for SIRTF, and, in fact, $< 10e^-$ RMS would be highly desirable. It is here that the present InSb arrays and MOSFET readout are lacking. We have been able to achieve a reproducable $200e^-$ RMS (corresponding to 63 μV at the InSb input) read noise in the lab and at the telescope, but efforts to reduce this further have not been succesful to date.

In what follows we will only discuss our results using the correlated triple sampling method which is appropriate for the source-follower amplifier per detector, direct readout (DRO) multiplexer which has been used for these tests. A measurement of signal begins by resetting the integration node to its starting value. The output voltage with the reset switch closed is called the reset or "R" level. We label this reset level R_1, corresponding to the first read cycle. Then the reset switch is opened and the integration begins. There is typically a small (few mV) jump in output voltage when the switch is opened; the new output voltage, at the beginning of the integration, is called the pedestal or "P_1" level. During the integration, the nodal capacitance, which is composed of the InSb diode capacitance plus the detector gate and MOSFET gate capacitances, is discharged by the photocurrent and dark current. At the end of integration, the output is read again. This level is called the signal or "S_2" level. Then the cycle is repeated. If succesive cycles are labelled 1, 2, 3 etc., then a good first approximation of the net signal due to photocurrent and dark current during the integration time is $S_2 - P_1$. This differential measurement eliminates DC offsets and the noise incurred when resetting the node (a minimum of $\sqrt{kTC}$). However, since the time between 1 and 2 can be very long, say 500 sec. for a deep SIRTF integration, this measurement is prone to $1/f$ drifts in the various circuit elements. We monitor this drift by also measuring the reset levels at the beginning and end of the integration. The quantity $(S_2 - P_1) - (R_2 - R_1) = (S_2 - R_2) - (P_1 - R_1)$ is formed, which should also eliminate the $1/f$ drift in the amplifier chain. This is called correlated-triple-sampling, though it probably should be called quadruple sampling. A factor of 2 increase in noise, compared to only sampling the signal levels, is accepted in order to remove the $1/f$ and resetting noises. Using this technique, we have found no increase in read noise going from 0.1 sec to 500 sec. integrations (with a constant pixel sampling time).

One source of $1/f$ drift which is not eliminated by this technique is variation in the DET SUB and VRSTUC supplies, which determine the bias across the detector after resetting. Drifts in these supplies will come through with full force. However, since all 58 × 62 detectors use the same DET SUB and VRSTUC supplies, this will result in an overall level shift of all the pixels on the array, rather than pixel to pixel noise. This probably explains the anomalous negative dark currents seen, as described previously. The negative 400 electron dark charge seen corresponds to a drift of 0.1 mV in the supplies during the 500 sec. integration. For SIRTF, the supplies should be made more stable than this.

We have compared our observed read noise to the theoretically expected read noise. We use the theory presented by Janesick *et al.* (1984), extended for correlated triple sampling. The theory takes as input the voltage noise spectrum of the MOSFET amplifiers. For our arrays we have measured a white noise floor of $76nV/\sqrt{(Hz)}$ and a $1/f$ noise of

$4\mu V/\sqrt{(Hz)}$ at 1 Hz at low temperatures $(6-10K)$. These were measured at the array output. The DC gain of the array MOSFETs is measured to be 0.8 at low temperatures. For optimal signal-to-noise ratio, a bandwith limiting RC filter of time constant $\tau = t/2$, where t is the "clamp-to-sample" time, is called for (Janesick *et al.* 1984). In our case t is the duration of the signal, reset, and pedestal levels. Thus for a 36 μsec/pixel read period, $t = 10.7\mu$sec is used (the extra 4 μsec are due to overhead). The voltage sampling function H(f) for an integration time T is given by:

$$H(f) = 2\frac{(1-\cos(2\pi ft))}{1+(2\pi f\tau)^2}2[1-\cos(2\pi fT)]$$

Because in all case T is at least 6000 times t (there being 1798 pixels to read out on each of the 2 outputs), the last term is a very rapidly oscillating function which averages to 2, giving effectively:

$$H(f) = 4\frac{1-\cos(2\pi ft)}{1+(2\pi f\tau)^2}$$

This function is multiplied by the square of the MOSFET voltage noise and integrated over all frequencies. The square root of this latter quantity gives the predicted RMS read noise at the array output. Dividing by the DC gain of 0.8 and the gain of the RC filter (0.86) gives the noise referred to the InSb input, δV. By operating our arrays at 350-400 mV of back bias, we reduce the nodal capacitance (dynamic) to $C' = 0.5$pF. The read noise in electrons will be:

$$\delta Q = C'\delta V \tag{5}$$

READ NOISES AT InSb INPUT

pixel time (μsec)	t (μsec)	f_{peak} (kHz)	RMS read noise Theory δV (μv)	Theory δQ (e^-)	Observed δV (μV)	Observed δQ (e^-)
36	10.7	33	46	146	79	250
$\geq$576	$\geq$171	≤ 2	12	38	63	200

The quantity f_{peak} is the frequency where the largest contribution to the read noise occurs. At fast pixel read times, i.e. 36μsec/pixel, the theoretical read noise is limited by the white noise floor near 33kHz. The observed read noise is somewhat less than a factor of 2 above this. At slow pixel read times, i.e. $\geq$ 576 μsec/pixel, The MOSFET $1/f$ noise results in a minimum read noise of $12\mu V$ RMS; however, the best observed read noise is about 5 times higher than this. We have not been able to determine the origin of this excess read noise. In the absence of a solution to this problem, we recommend employing lower capcitance pixels to reduce the read noise in electrons as given by equation (5).

Non-Linearity/Calibratibility

It is important that the output of the array be calibratible to achieve a high level of photometric accuracy. We anticipate observing using a wide range of integration times and signal levels and wish to calibrate these data based on measurements of objects of known brightness. Our system permits selection of a large number of different data taking modes: correlated double sampling ($S_2 - R_1$) and correlated triple sampling with pixel read times ranging from 18μsec/pixel to 1152μsec/pixel, operating under both high background ($\lambda > 3\mu m$) and low background ($\lambda < 2.5\mu m$) conditions.

The output of our array is inherently non-linear primarily because of the voltage dependent capacitance of the InSb diodes. The dynamic capactance of an abrupt-junction, low temperature InSb diode is given by

$$C'_{InSb} = \frac{dq}{dV} = \frac{C'_0}{\sqrt{1 + V/V_{bi}}} \tag{6}$$

where q is the stored charge, V is the back bias, $V_{bi} \approx$0.24V is the built-in junction voltage. For our pixels (62μm square junctions, $2 \times 10^{14}/cm^3$ doping) we estimate the zero-bias dynamic capacitance $C'_0 = 0.41pF$. The total capacitance of the integrating node will be the sum of this plus the fixed capactance due to the MOSFET gate, detector gate, and In bump bonds. We estimate this at:

$$C'_{fixed} = C_{fixed} \simeq 0.23pF$$

The total dynamic capacitance will be

$$C'_{tot} = C'_{fixed} + C'_{InSb}$$

This dynamic capacitance immediately gives the noise in electrons from the measured voltage noise δV through equation (5).

For estimates of the QE, we need the effective <u>*static*</u> capacitance, defined through

$$q(v) = q_o + \int_o^v C'_{tot} dV \tag{7}$$

where q_o is the charge stored on the InSb junction at zero bias. Defining Q as the difference in charge:

$$Q \equiv q - q_o \tag{8}$$

and C as the effective static capacitance:

$$C \equiv \frac{1}{V} \int_o^v C'_{tot} dV \tag{9}$$

We recover the familiar:

$$Q = CV \tag{10}$$

Q versus back-bias V is plotted in figure 12. This shows the slight non- linearity expected. The total effective capacitance versus V is plotted in figure 13. The dynamic capacitance C' is given in figure 14 and compared to the static capacitance. At zero detector bias, the dynamic and effective static capacitance are equal. Figure 14 shows that read noise (equation (5)) can be reduced by employing a large back bias to reduce the dynamic capacitance. We typically employ 350-400 mV of back bias which reduces C' to 0.5 pF from its zero bias value of 0.64 pF.

We have had three observing runs, in June 1988, July 1988, and September 1988, where data was taken to calibrate the system non-linearity. In order to emphasize the deviations from linearity, we plot the signal divided by integration time (ITIME). According to the capacitance model above, we expected to see a constant value for this at short ITIME's, and a droop downward as the InSb diode becomes discharged, increasing its capacitance, at longer ITIME's. A sampling of the actual data is given in figure 15. We analyze the 62 pixels in row 52, which has about a factor of 2 variations in QE from one end to the other. In the plots, full scale is $\sim 10 - 20\%$ variation in signal/ITIME.

From these graphs, an anomalous increase of a few percent in signal/ITIME is seen for the first few ITIME's in many of the time series. (ITIME = 60 for a one second integration). This has happened at pixel read times ranging from 18 μsec (2 Rate, 2/60 sec. to read out the array) to 288 μsec (32 rate, 32/60 sec to read out the array), using both correlated double and triple sampling. Apparently, the array takes a little (integration) time to get up to speed. We are currently studying this effect further, but have no bright ideas yet. This effect could introduce a few percent uncertainty in calibrated fluxes.

At longer ITIME's, the plots show the droop expected, from capacitance increase. In order to be able to use a large number of pixels, each with different signal levels, to generate a non-linearity calibration curve, we form the logaritmic derivative:

$$\frac{dlog(signal)}{dlog(ITIME)} = \frac{dlogS}{dlogt} \tag{11}$$

and plot it versus signal S. A signal of 16,500 counts here corresponds to capacitance discharge of $10^6 e^-$. The logarithmic derivative has the property of being 1 if the output is exactly linear. It basically gives the slope on a log-log plot of S $\underline{vs}$ t. Figure 16 gives a typical result. Values near 1 are seen at low signals and a drop down to 0.8 is seen near 16,500 counts of signal. The data has been fit with a quadratic function:

$$\frac{dlogt}{dlogS} = 1 + 0.08(\frac{S}{10^4})^2 \tag{12}$$

which is also shown in the plot. Equation (12) can be immediately integrated to give a "linearized" signal Q which is proportional to the charge accummulated:

$$Q = Se^{0.04(S/10^4)^2} \tag{13}$$

This is plotted in figure 17. About 10% droop in S/Q occurs at 16,500 counts ($\sim 10^6 e^-$).

The capacitance model described above has been compared to this data. We estimate the initial detector back bias is $\simeq$400 mV when we have applied 300 mV of back-bias

through the CRC 228 readout (the source of this offset is not understood at this time). Using this value, the expected logarithmic derivative and linearization factor S/Q are given in figure 18, compared to the data and the numerical fit. Only fair agreement is seen. Some of the effects which could contribrute to such a discrepancy are:

a. Back-bias really lower than the 400 mV assumed.

b. The fixed capacitance is lower than the 0.23 pF assumed

c. The gain of the signal chain is off by several percent.

In addition, a non-abrupt InSb junction may exhibit different non-linearity characteristics.

We estimate that the uncertainty in fluxes introduced by our incomplete knowledge of the hybrid array and associated electronics is a few percent. Flat-fielding, described below, is potentially more limiting.

Flat Fielding

The images obtained when observing a uniformly bright screen (figs 1 & 3) show large variations. There are prominent "tree rings" as well as an overall gradient from left to right. In order to calibrate these effects out of our images, we obtain images of candidate flat fields, which we will (after linearization) divide into our astronomical images. In addition, we desire the flat fields to represent as nearly as possible the same optical illumination of the array as the astronomical images. In the past, we have used the moon as a candidate flat field. With the current array, the moon is too bright at most wavelengths. Therefore, the 1.25-2.5μm region we have taken images of the evening or morning blue sky and the inside of the dome illuminated by 5000 W of incandescent lamps. For the thermal infrared ($\lambda > 2.5\mu m$), we image the inside of the dome and subtract the image of blank sky. The last step eliminates the thermal emission from the mirrors, etc., which does not represent the same optical illumination of the array as our astronomical images.

In order to test our candidate flat fields for photometric accuracy, we have imaged two calibration stars at 25 different positions on the array. Figure 19 summarizes the photometric results at $2.23\mu m$. With no flat field correction, there is a large standard deviation of 21% of the mean, due primarily to the gradient in QE. Using a flat field composed of comparable parts of dome plus blue sky (they were very similar in appearance) improves the standard deviation to 4.5%. With this data, a systematic pattern can be seen. A minimum in counts is seen near the center of the array (x's) and a maximum is seen near the peripheries (+'s). We attribute this to the effects of plate scale distortion caused by our re-imaging optics. These optics give a small amount of pincushion distortion. This means the arcsec/pixel plate scale is *smaller* near the peripheries than on the optic axis. This *reduces* the signal from the flat field near the peripheries. However, the signal from the star is not reduced because a large aperture ($\sim$ 9 pixel square box) is used to include all the star's signal. Therefore the flat field for stellar photometry differs from a flat field appropriate for extended emission (such as the dome and blue sky). In order to account for this distortion effect in stellar photometry, the flat field was divided by an optics correction

factor f:

$$f = 1 - \epsilon\rho_{41}^2 \tag{12}$$

This being the simplest function of the nature suggested by the optics distortion. ρ_{41} is the distance from the optic axis at row R_o, column C_o normalized to a distance of 41 pixels (i.e. the corner of the array). ϵ is the magnitude of flat field correction. By varying the three parameters ϵ, R_o, and C_o a minimum of 2.6% in the standard deviation of the stellar signals was achieved. The optic axis was found to be at row 42 ± 4, column 26 ± 5 which is believable. This is displaced 14 pixels or 1.06mm from the array center. The magnitude ϵ was 0.10, i.e., a 10% effect 41 pixels away from the optic axis (the array corner). Ray tracing of the optics gives a plate scale distortion resulting in a flat-field correction function nearly identical to equation (12), but with a 10% smaller ϵ. This supports the interpretation offered above.

We estimate a net uncertainty in stellar photometry of about 3.5% due to flat fielding and linearization uncertainities. For typical ground based observing, a net accuracy of 5-10% should be achievable.

For SIRTF, more study (or better-behaved detector and optics) would be necessary to surpass 3.5% photometric accuracy.

References

Fowler, A. M., Probst, R. G., Britt, J. P. Joyce, R. R., and Gillett, F. C., 1987 "Evaluation of an Indium Antiminide Hybrid Focal Plane Array for Ground- Based Astronomy", Opt. Eng. **26**, #3, p. 232 (March 1987)

Orias, G., Hoffman, A. W. and Gasselman, M. F., 1986, "58 × 62 InSb Focal Plane Array for Infrared Astronomy" Proc. S.P.I.E, **627**, p. 608 (March 1986)

Ninkov, Z., Forrest, W. J., and Pipher, J. L., 1987, "Testing of a 58× 62 InSb Engineering Array" in Infrared Astronomy with Arrays ed. C. G. Wynn-Williams and E. E. Becklin (U. Hawaii, Institute for Astronomy, Honolulu, Hawaii)

Janesick, J. R., Elliott, T., Collins, S., Marsh, H., Blouke, M., and Freeman, J., 1984, "The Future Scientific CCD", S.P.I.E. Proc. Vol. 501, p.2.

Sze, S. M. 1981 "Physics of Semiconductor Devices, 2nd Ed." (John Wiley & Sons, NY).

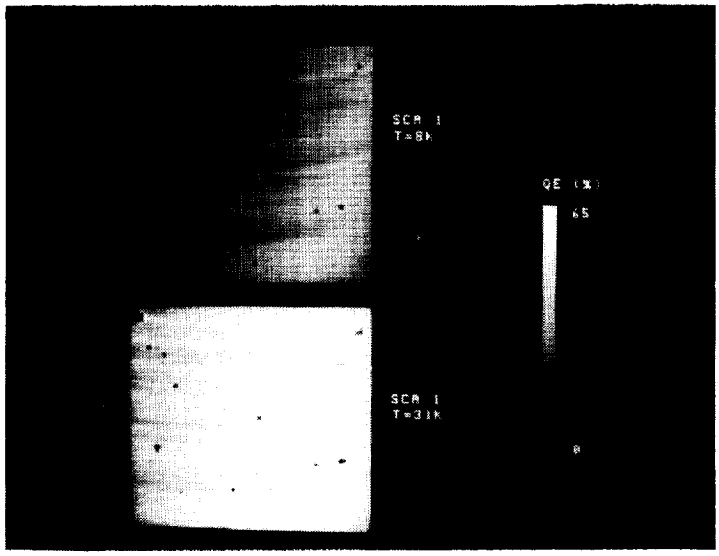

Fig. 1 - Gray Scale representation of Quantum efficiency measurement of SCA 01 at 31 K and 8 K.

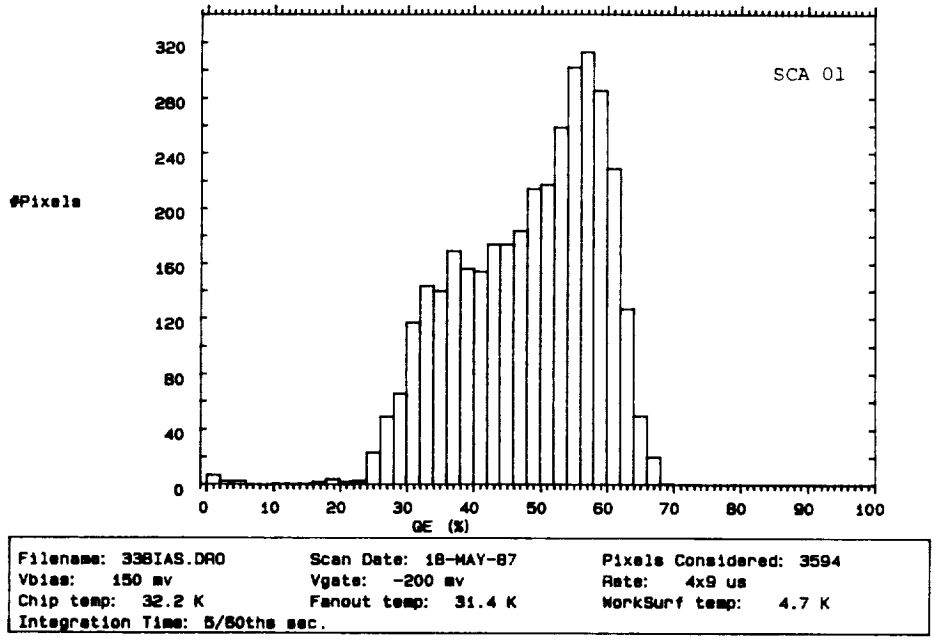

Fig. 2a- Histogram of Quantum Efficiency measurements at 31 K. Assumed zero-bias capacitance was 0.63 pF. Illumination through narrowband 3.3 micron filter; room irradiance.

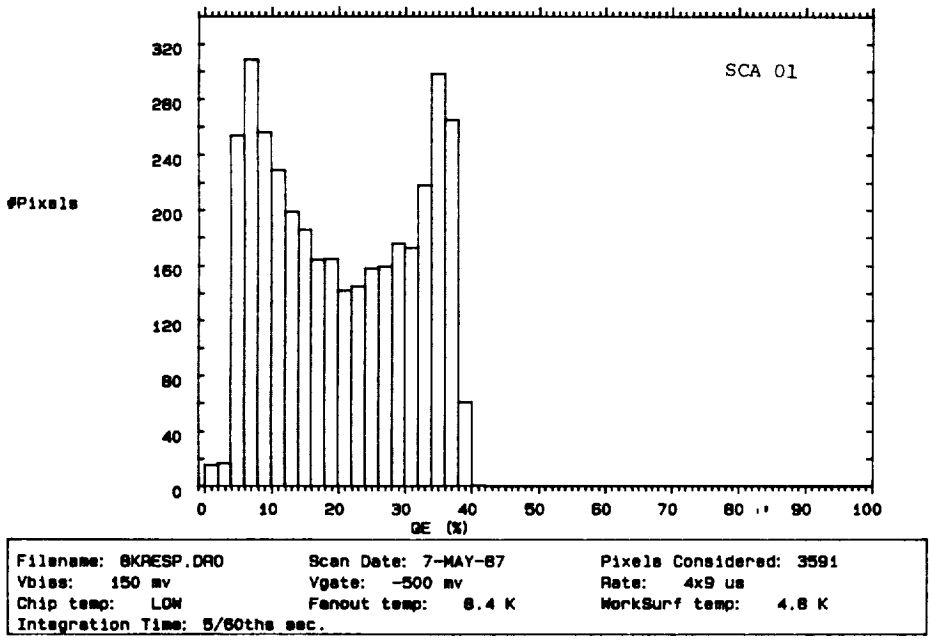

Fig. 2b- Histogram of Quantum Efficiency measurements at 8 K. Other conditions as above.; assumed zero-bias capacitance was 0.55 pF.

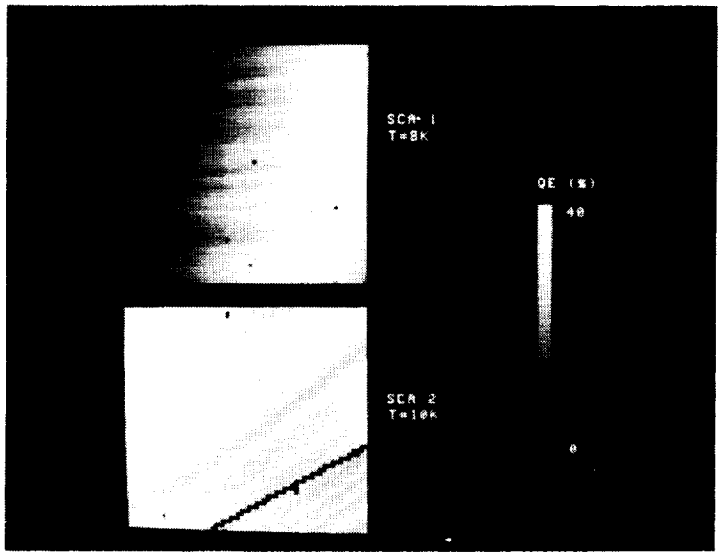

Fig. 3. Gray scale comparison of quantum efficiences of SCA 01 and SCA 02.

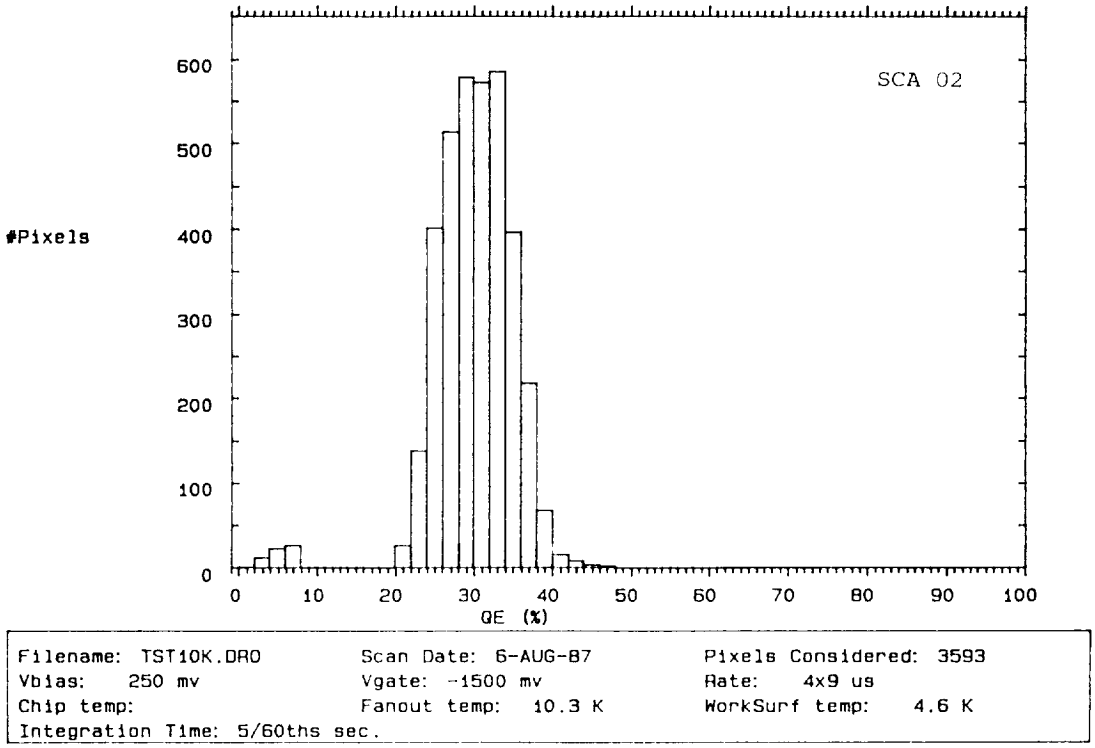

Fig. 4. - Quantum efficiency of SCA 02 at 10 K and 3.3μm.

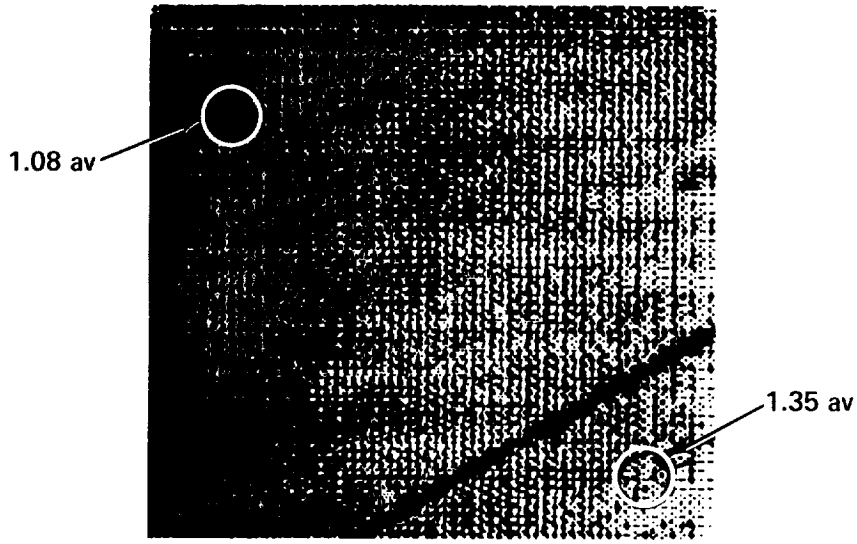

Figure 5. Flat fields for SCA 02 at 3.3 microns. 10 K flat field divided by 7 K flat field showing loss of QE in the lower right corner as the temperature of the InSb is decreased. The QE ratio 10K/8K ranges from 1.35 in the lower right corner to 1.08 in the upper left corner. The dark diagonal line in the lower right is due to approximately 40 permanently dead pixels. They have extremely high dark currents.

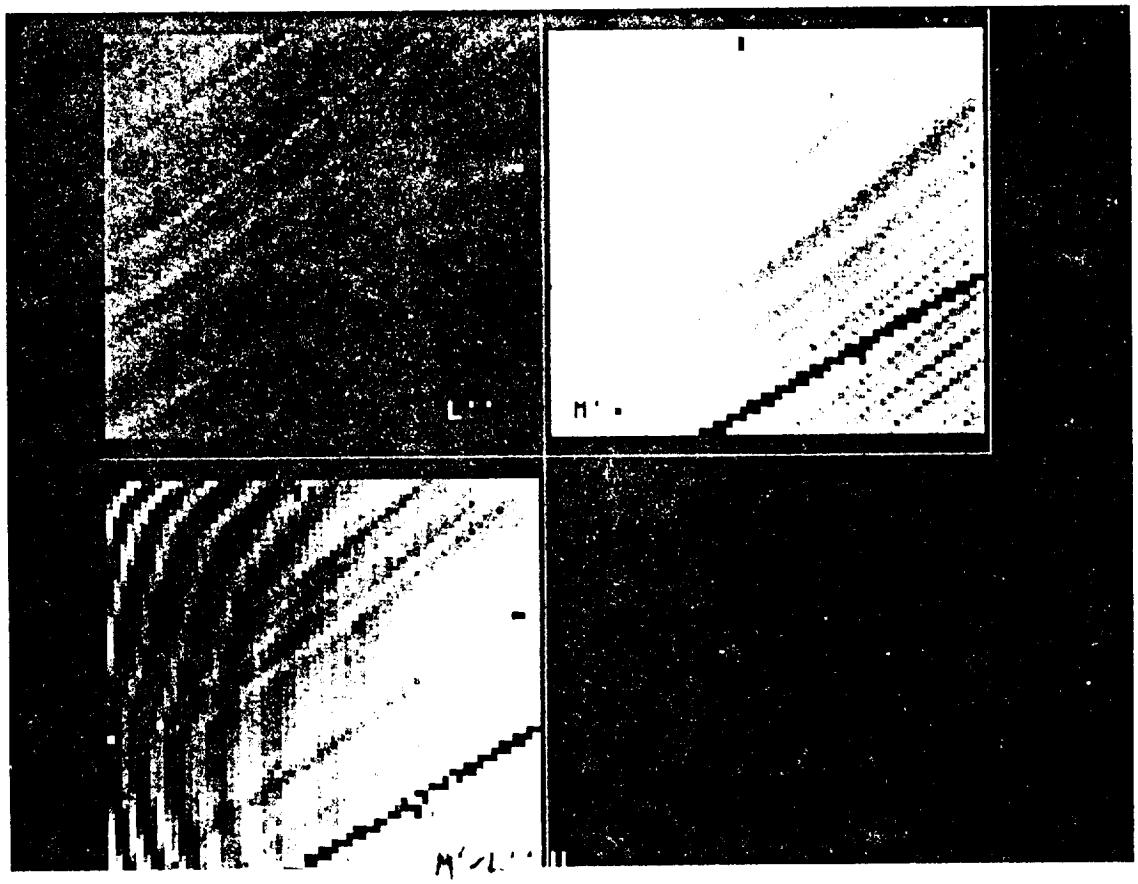

Figure 6. Flat fields for SCA 02. Upper left is at 3.75 μm (L'') through a 22% resolution filter and upper right is through a 4.67 μm (M'), 4% resolution filter. The M' image shows the interference fringes, primarily because of the greater penetration of 4.67 μm photons into InSb. In the lower left, the M'/L'' ratio image shows the interference fringes more clearly. Each fringe corresponds to a change in thickness of 0.6 μm, as described for figure 5a. The greater number of fringes for SCA 02 compared to FPA 72 indicates a greater thickness variation, especially on the left hand side. The more distinct fringes on the left are believed to be from the thinner side. This side also exhibits higher quantum efficiency at these low temperatures, as shown in the upper two images.

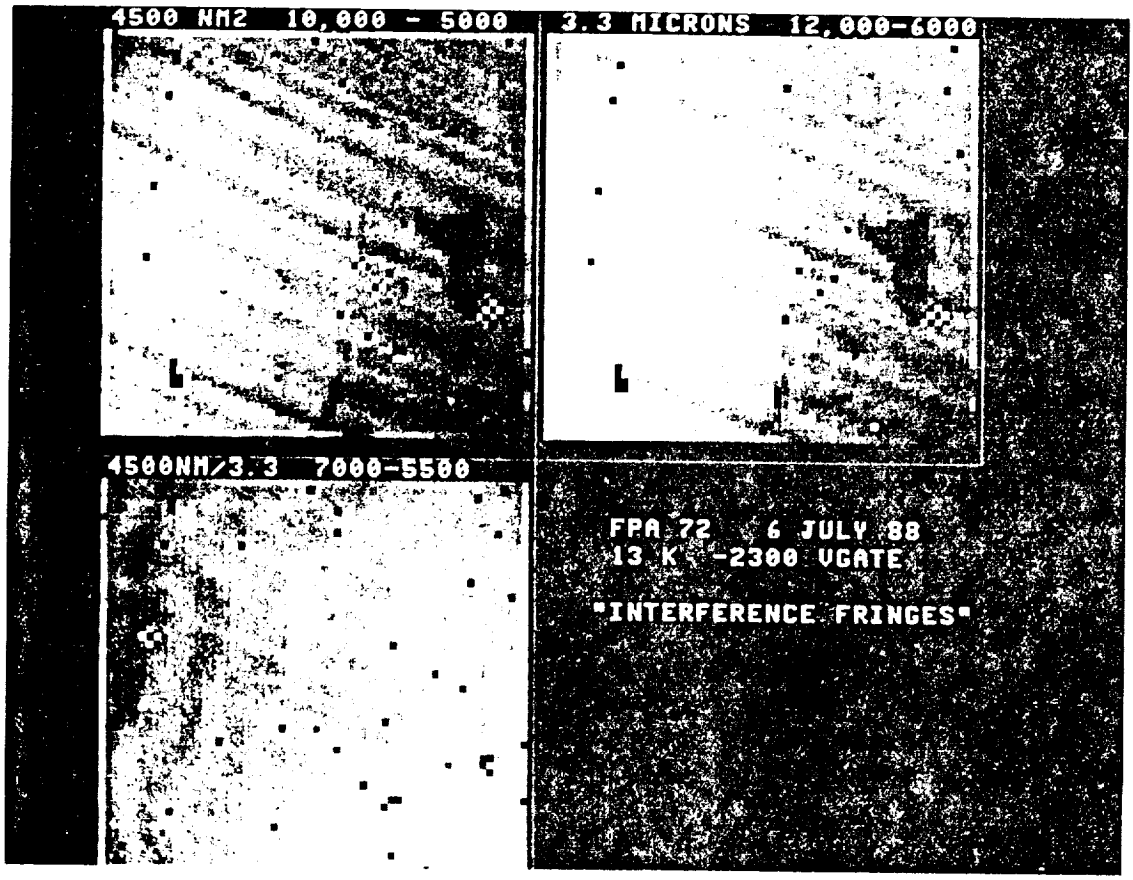

Figure 7. Flat fields for FPA 72. Upper left is at 4.5 microns through a 1% resolution CVF. Upper right is at 3.26 microns through a 7% resolution interference filter. Lower right is the ratio of the 4.5 to 3.26 micron flat fields. We interpret the alternating dark and bright wavy lines as interference fringes in the 4.5 micron radiation. A bright peak is seen whenever the detector thickness equals $m\lambda/2n$, where m is the order, λ is the wavelength, and n=3.8 is the index of refraction of InSb. Adjacent bright lines differ by 1 in m.

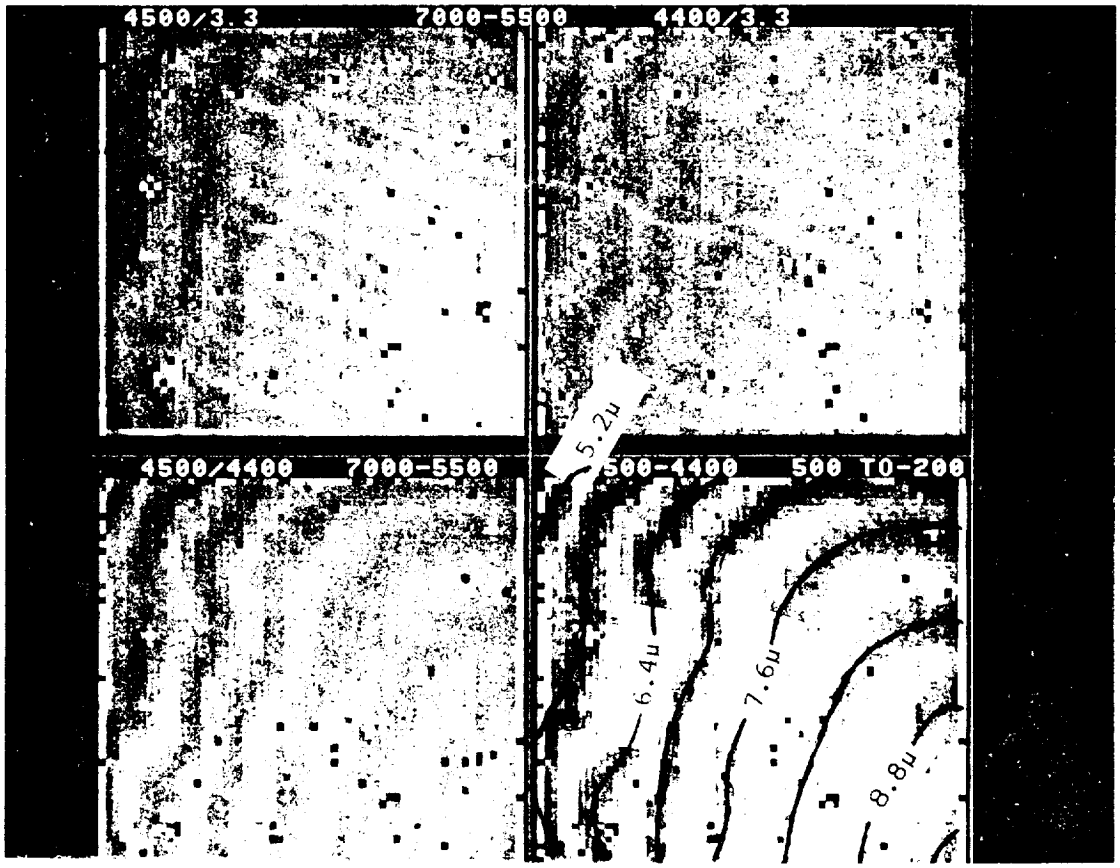

Figure 8 Flat fields for FPA 72. The 4.5μm/3.3μm (upper left) and 4.4μm/3.3μm (upper right) show the interference fringes described for Figure 5a. Note that the fringes are shifted a bit to the right at the longer wavelength, showing that the thickness is increasing in that direction. The lower two images are 4.5μm/4.4μm and 4.5μm - 4.4μm images, which show the fringes more clearly. The detector thickness for selected fringes is indicated on the lower right image.

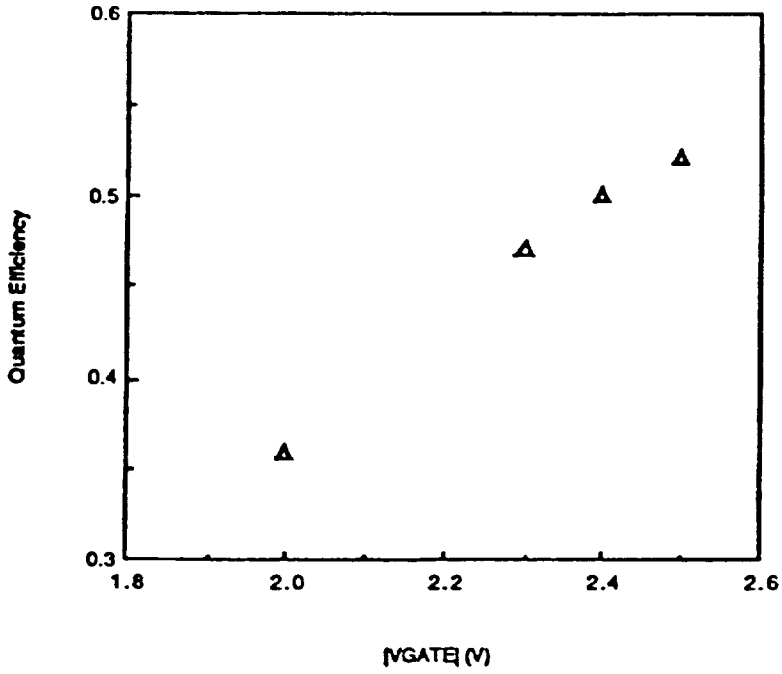

Fig. 9 The effect of gate voltage on average 3.3 μm quantum efficiency. These data were taken on device FPA 72, which was antireflection coated. The temperatures were 9 and 10 K.

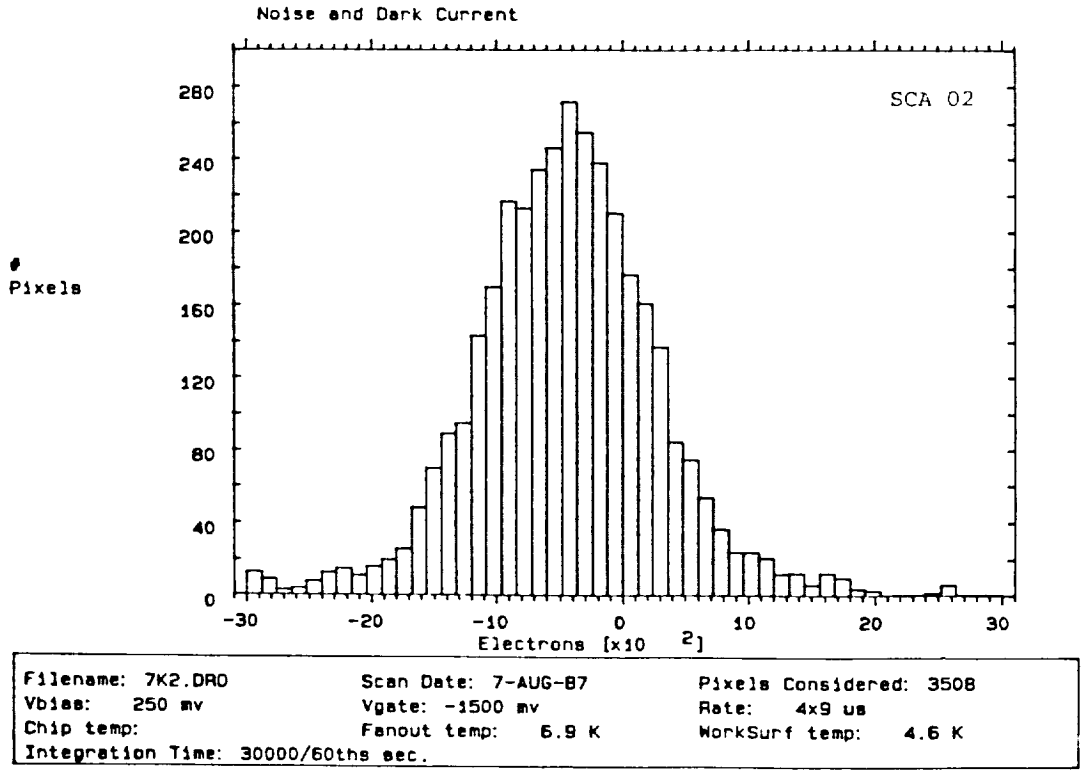

Fig. 10 - Dark charge in SCA 02 after 500 sec. The spread in the measurements corresponds to approximately 300e- RMS noise.

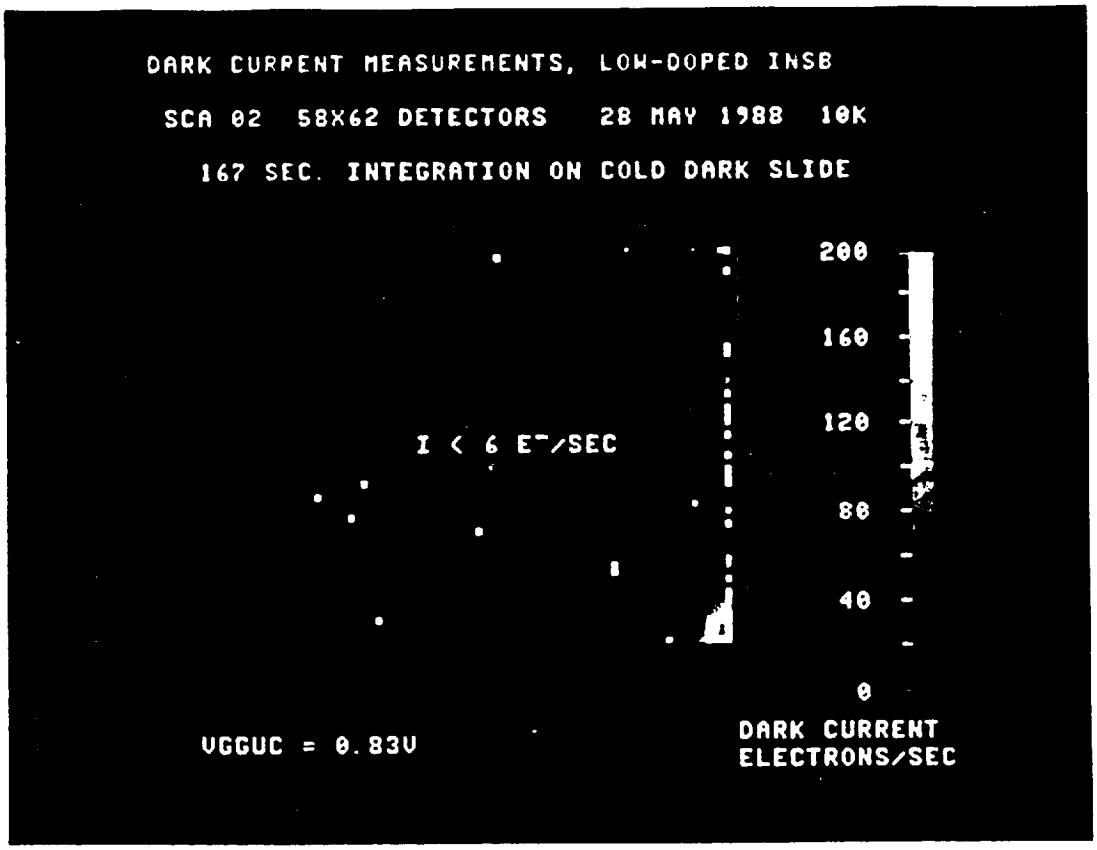

Fig. 11. Dark current in SCA 02 at 10 K. Only an upper limit of less than 6 e-/sec could be established in the central 95% of the array. The glow in the lower right corner may be an LED effect from the output amplifiers, which are located in this vicinity.

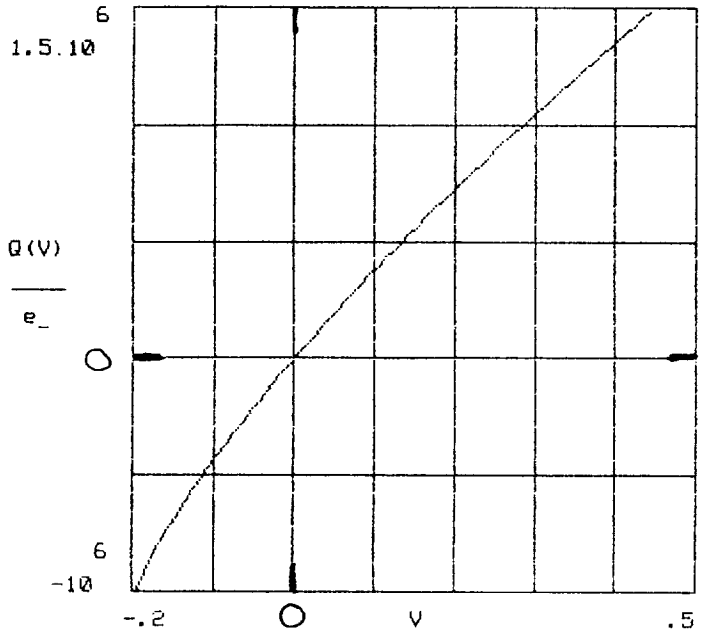

Figure 12. Effective charge stored Q vs. actual detector back-bias V. This plot is a little more linear than the earlier version. Also note the availability of negative back-bias to increase dynamic range.

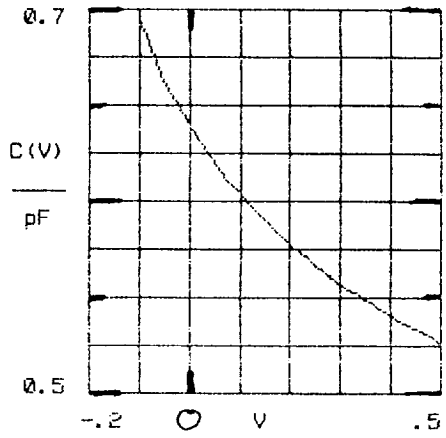

Figure 13. Effective capacitance C vs. detector back bias V. Since Q = CV, this shows the non-linearity more clearly.

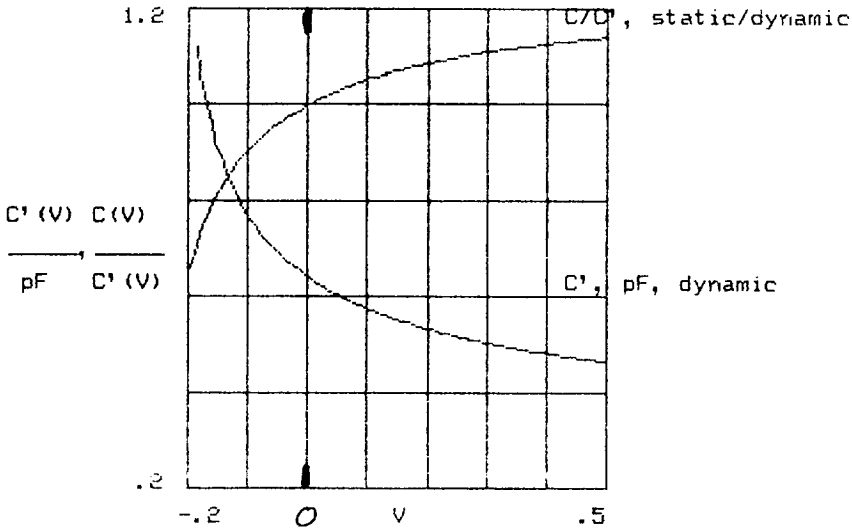

Figure 14. Dynamic capacitance C' vs. back-bias V. Since $\delta Q = \delta V(dQ/dV) = \delta V * C'$, this capacitance determines the electron read noise. Also included is a comparison the static capacitance C to C'.

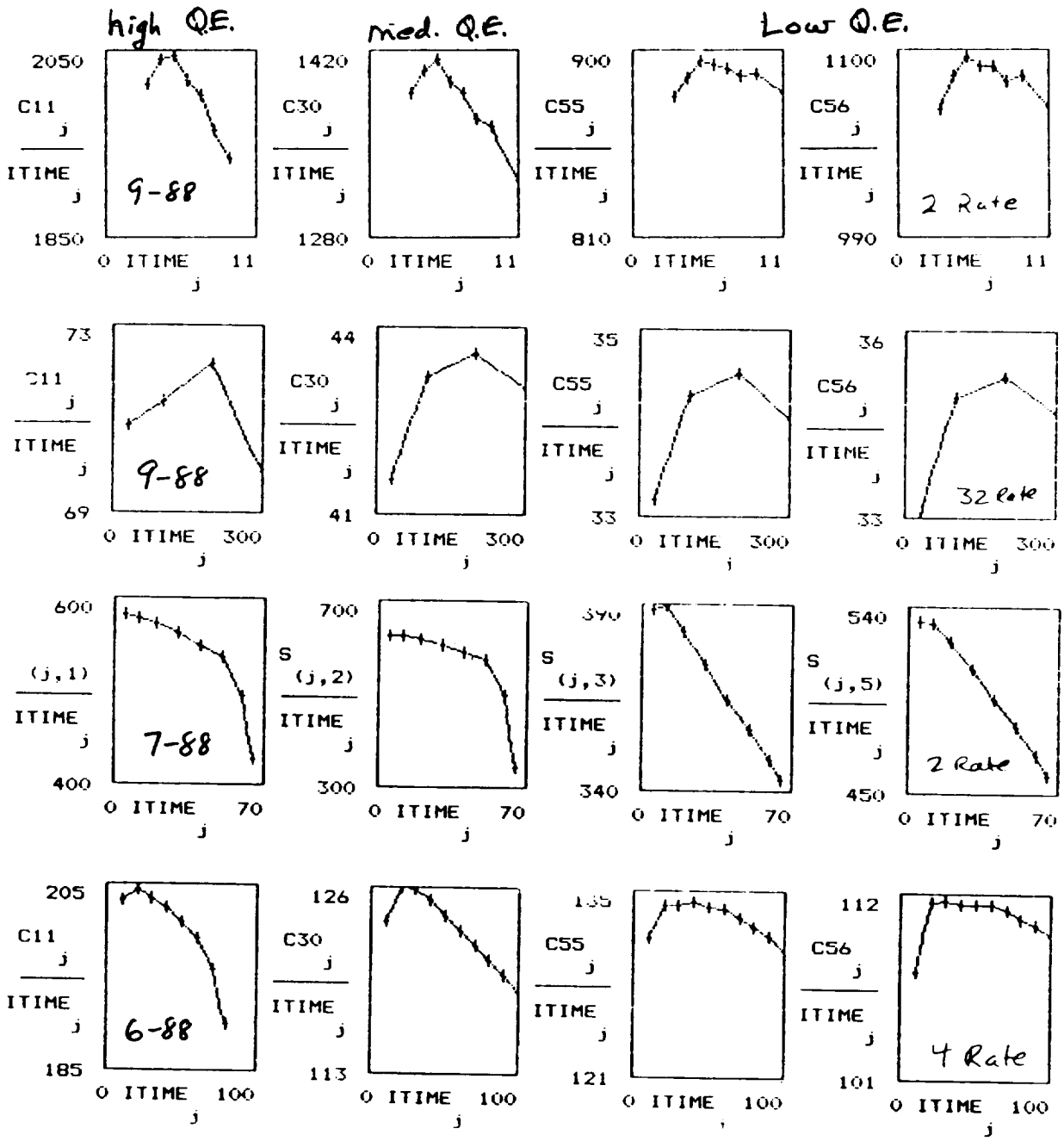

Fig. 15. Signal divided by integration time (ITIME) versus ITIME for pixels 11, 30, 55, and 56 in row 52 of InSb array SCA 02. In all cases, the detector viewed a constant brightness flat field. Data from June, July and September 1988. Detector temperature 10 to 12 K. Pixel read times from 18 μsec (2 Rate) to 288 μsec (32 Rate). The leftmost column is the highest QE pixel and the rightmost column is the lowest QE pixel. The anomalous rise often seen at short ITIMEs is not understood. The droop at longer ITIMEs is analyzed in figs. 16 and 18.

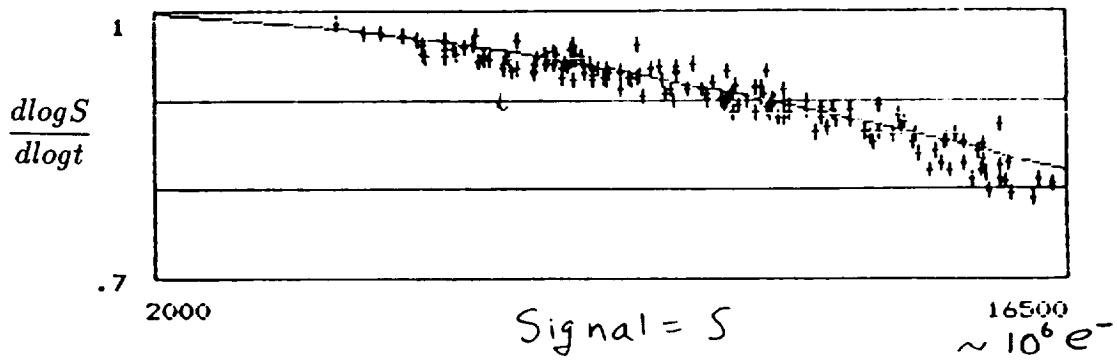

Fig. 16. Logarithmic derivative (see text) versus signal data (crosses) for SCA 02, row 52 pixels. Representative raw data is shown in the first row of fig. 15. The line is a quadratic fit to the data.

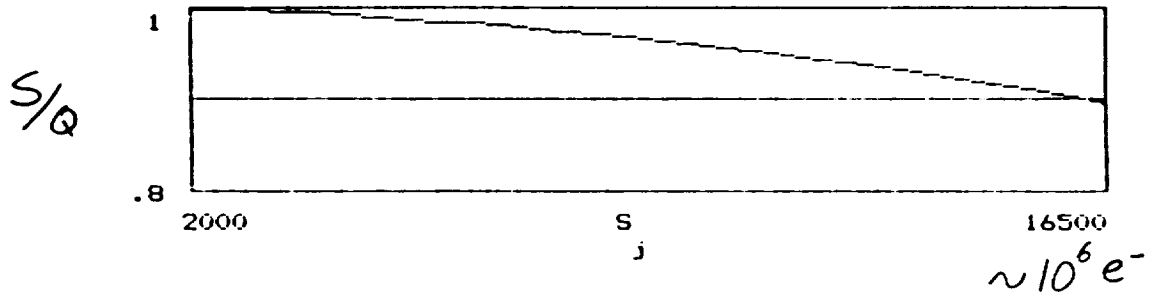

Fig. 17. Linearization factor S/Q versus signal S from the fit to the logarithmic derivative shown in fig. 16 (see text).

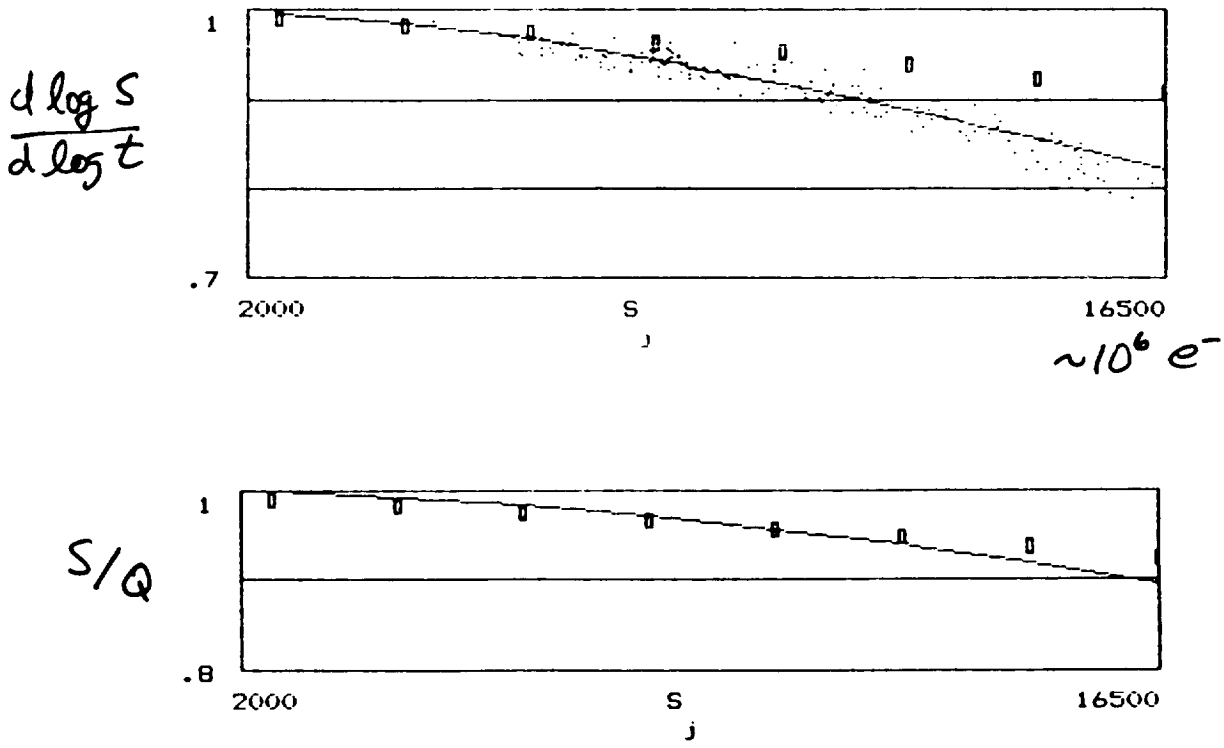

Fig. 18. Capacitance model (boxes) compared to the data (points) and empirical fit (lines) from figs. 16 and 17 (see text).

÷ const.

Key:
X's = low < –4%
+'s = high > +4%
boxes = ave ±4%

$\sigma = 21\%$

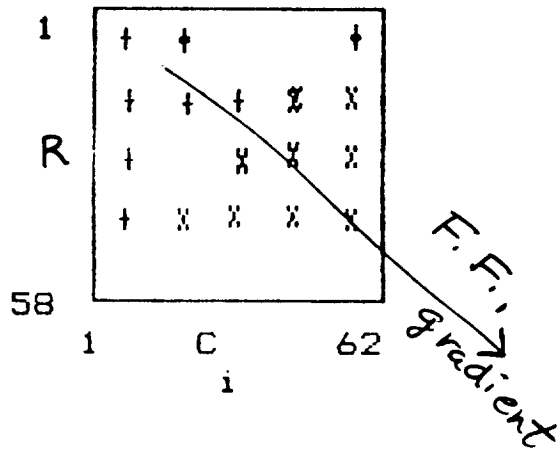

÷ (blue sky + dome)

$\sigma = 4.5\%$

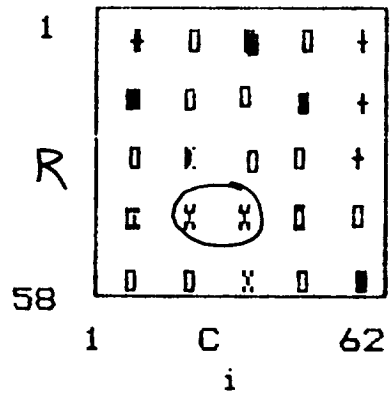

Optics correction (p.s. distortion)
$f = 1 - \epsilon\rho^2$
$\epsilon = \frac{0.1}{41^2}$
Ctr @ Row 42 Col 26

$\sigma = 2.6\%$

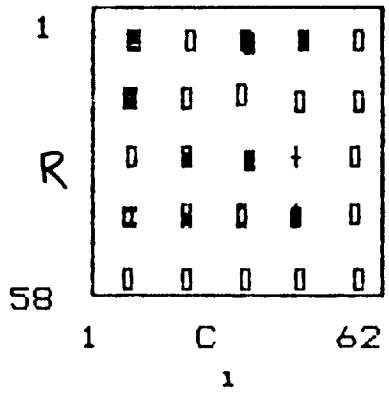

Fig. 19. Tests of photometric accuracy using the infrared standard star HD 40335 in Sept. 1988 at the IRTF. The star was imaged twice at each of 25 positions on the array. The images were divided by a candidate flat field and the signal in a 9 pixel (3.8") octagon was summed to give the total signal. The signal at each position is compared to the average for all positions with the key as shown in the figure. The top figure is with no flat field correction. The standard deviation was 21% of the average. The middle figure used the blue sky and dome as a flat field, improving the standard deviation to 4.5%. The bottom figure includes the optics correction (see text) with further improvement to 2.6% standard deviation.